Radio Science

RESEARCH ARTICLE

Key Points:

- A method to determine the azimuthal angle of arrival and azimuthal extent of E-region coherent scatter was developed for the Ionospheric Continuous-wave E-region Bistatic Experimental Auroral Radar (ICEBEAR)
- The azimuthal angle and extent of targets were found using Gaussian fits to cross-spectra coherence data from a linear receiving array
- Data from ICEBEAR in the linear receiving array configuration can use this imaging method to accurately map the data

Correspondence to:
D. Huyghebaert,
devin.huyghebaert@usask.ca

Determination of the Azimuthal Extent of Coherent E-Region Scatter Using the ICEBEAR Linear Receiver Array

Devin Huyghebaert[1] ⓘ, Kathryn McWilliams[1] ⓘ, Glenn Hussey[1] ⓘ, Draven Galeschuk[1], Jorge L. Chau[2] ⓘ, and Juha Vierinen[3] ⓘ

[1]Department of Physics and Engineering Physics, University of Saskatchewan, Saskatoon, SK, Canada, [2]Leibniz Institute of Atmospheric Physics, University of Rostock, Kühlungsborn, Germany, [3]Department of Physics and Technology, UiT-The Arctic University of Norway, Tromsø, Norway

Abstract The Ionospheric Continuous-wave E-region Bistatic Experimental Auroral Radar (ICEBEAR) is a VHF coherent scatter radar that operates with a field-of-view centered on 58°N, 106°W and measures characteristics of ionospheric E-region plasma density irregularities. The initial operations of ICEBEAR utilized a wavelength-spaced linear receiving array to determine the angle of arrival of the ionospheric scatter at the receiver site. Initially only the shortest baselines were used to determine the angle of arrival of the scatter. This publication uses this linear antenna array configuration and expands on the initial angle of arrival determination by including all the cross-spectra available from the antenna array to determine both the azimuthal angle of arrival and the azimuthal extent of the incoming ionospheric scatter. This is accomplished by fitting Gaussian distributions to the complex coherence of the signal between different antennas and deriving the azimuthal angle and extent based on the best fit. Fourteen hours of data during an active ionospheric period (March 10, 2018, 0–14 UT) were analyzed to investigate the Gaussian fitting procedure and determine its feasibility for implementation with ICEBEAR. A comparison between mapped scatter, both neglecting azimuthal extent and including azimuthal extent is presented. It demonstrates that the azimuthal extent of the ionospheric E-region scatter is very important for accurately portraying and analyzing the ICEBEAR measurements.

1. Introduction

Ionospheric coherent scatter radars make measurements of plasma density irregularity characteristics in the terrestrial ionosphere. The plasma density irregularities can exist over a large portion of the radar field-of-view (FOV) resulting in scattered signals arriving at the receiver from multiple directions simultaneously when using wide beam transmitter antennas. It is possible to "image" the incoming radar signal and determine where the signal is scattered through the use of interferometric radio techniques with multiple antennas. By imaging the incoming signal, a better representation of the scattering region can be determined, providing details on the size of the region in which plasma density irregularities are present.

The Ionospheric Continuous-wave E-region Bistatic Experimental Radar (ICEBEAR) (Huyghebaert et al., 2019) is a coherent scatter radar that measures characteristics of plasma density irregularities in the E-region ionosphere with a FOV in the terrestrial auroral zone. The initial operations of this radar utilized a linear receiving array to determine the azimuthal angle of arrival of the incoming scattered signal. A more accurate azimuthal angle of arrival and details about the size of the scattering region in azimuth can be determined through the use of the larger baselines, where the ICEBEAR receiver antenna array consists of 10 antennas in a line with 6 m (one wavelength) spacing. This provides antenna baselines of 6–54 m in 6 m increments. The study presented here utilized the multiple baselines in the analysis of the azimuthal angle of arrival to better represent the size of the scattering region in the FOV. This has implications for understanding plasma density irregularity generation in the terrestrial ionosphere and the extent of ionospheric heating caused by plasma turbulence.

1.1. Science Background

The E-region ionosphere is a very complex region due to the characteristics and interactions between atmospheric species at this altitude. Some of the interesting characteristics of the atmospheric species in this region include the charged particle gyrofrequency and the relative density. The E-region is located at approximately 90–150 km in altitude and its dynamics are driven by both neutral atmospheric constituents and electromagnetic forces acting on charged particles. Electrons and ions follow different motions due to their respective collision rates with the neutral atmospheric species, where the electrons typically follow electromagnetic forces and the ions are unmagnetized due to collisions with neutrals (e.g., Kelley, 2009). Due to the different motions of the charge carriers, current flows in this region when there are electric fields present. This current results in Joule heating in the E-region ionosphere (e.g., Hays et al., 1973). The heating can affect the circulation of plasma and neutral particles in the ionosphere (Rodger et al., 2001).

The heating observed in the ionosphere during enhanced electric field events is not fully accounted for by Joule heating mechanisms without anomalous electron heating effects (Schlegel & St.-Maurice, 1981; St.-Maurice et al., 1981; Wickwar et al., 1981). One possible explanation for the anomalous electron heating is wave-particle interactions due to plasma turbulence (St.-Maurice et al., 1981). A mechanism by which this plasma turbulence is generated in the E-region ionosphere is the Farley-Buneman, or modified two-stream, plasma instability (Buneman, 1963; Farley, 1963). This instability occurs when the electrons in the electrically charged fluid are moving at a speed greater than the ion acoustic speed with respect to the ions in the fluid. When this occurs, plasma density perturbations grow in amplitude and plasma turbulence is generated in the medium. For the electrons to be moving at speeds greater than the ion acoustic speed with respect to the ions, an enhanced electric field in the E-region ionosphere must be present. Models have shown that including the plasma heating due to the Farley-Buneman instability can have significant impact on the predictions of the model (Liu et al., 2016, 2018; Wiltberger et al., 2017). Effects of the added heating considered in the models include an increase in electron temperature (Liu et al., 2016), an increase in the Pedersen conductivity (Liu et al., 2016; Wiltberger et al., 2017), and a change in the phase speed of traveling atmospheric disturbances (Liu et al., 2018). Due to the potential impact of this anomalous plasma heating, it is important to better understand the location and spatial extent of the Farley-Buneman instability during active ionospheric conditions so that the heating due to this instability can be properly modeled.

Ionospheric coherent scatter radars can measure characteristics of plasma density fluctuations in the E-region ionosphere caused by plasma instabilities. The plasma density perturbations are aligned with the geomagnetic field and the bisector of the path of the radar signal must be perpendicular to these density perturbations for radio waves to be scattered to the radar receiver site (e.g., Haldoupis & Schlegel, 1993). From the received signals parameters of the target can be recovered, such as the relative Doppler velocity of the plasma density perturbations and the relative radar cross section of the scattering volume. Reviews of the coherent E-region ionospheric scatter measured by radars are included in Moorcroft (2002), Makarevich (2009), and Hysell (2016), where details about E-region coherent scatter were investigated and described using plasma instability theories. Some recent experiments investigating auroral E-region coherent scatter can be found in Hysell et al. (2012) and Chau and St.-Maurice (2016). Hysell et al. (2012) compared the E-region coherent scatter spectra and location to incoherent scatter radar and all sky imager data to derive electric field estimates from the coherent scatter spectra. Chau and St.-Maurice (2016) measured E-region coherent scatter during an extremely active event with a radar optimized for meteor detection resulting in novel high resolution measurements of E-region coherent scatter during active ionospheric periods. Building on previous discoveries, ICEBEAR was designed by using modern radio techniques to obtain simultaneous high temporal and spatial resolutions over a FOV located in the terrestrial auroral zone to expand upon the understanding of the Farley-Buneman instability (Huyghebaert et al., 2019).

In previous studies using coherent scatter radars to measure characteristics of E-region plasma density irregularities, there were four different "types" of coherent scatter spectra that were measured. These were labeled Type I, Type II, Type III, and Type IV (e.g., Moorcroft, 2002). Type I spectra have relatively narrow spectral widths and a Doppler shift of approximately the ion-acoustic speed. These Type I spectra have been widely accepted as being due to the Farley-Buneman instability. The other types of coherent scatter are less well-understood, though strong arguments have been made for the cause of these different types of coherent scatter spectra. Type II E-region coherent scatter spectra are broad in spectral width and have

a Doppler shift of around 0 Hz. One hypothesis is that these Type II spectra are due to secondary plasma density irregularity generation at directions perpendicular to the $E{\times}B$ drift direction created from primary waves propagating in the $E{\times}B$ direction (e.g., Hamza & St-Maurice, 1993).

Type III measurements have a narrow spectral width with a Doppler shift approximately half the ion-acoustic speed and Type IV measurements have a narrow spectral width with a Doppler shift of approximately double the ion-acoustic speed. It has been suggested that Type III are due to "Modulated Electron Ohmic Heating by Waves" and occur at the lower altitudes of the E-region (St.-Maurice & Chau, 2016). Some previous interpretations of Type III scatter include a 3-wave coupling process (Sahr & Farley, 1995), or that effects from the gradient drift instability lower the phase velocity of Type I scatter (Haldoupis et al., 1995). Type IV on the other hand have been suggested to occur at the higher altitudes of the E-region, where the ions are less coupled to the neutral atmospheric species and have a velocity component in the direction of the $E{\times}B$ drift. The plasma density irregularities generated from the Farley-Buneman instability propagate in the reference frame of the ions, resulting in the large Doppler shift observed by coherent scatter radars (St.-Maurice & Chau, 2016). Another explanation for Type IV E-region coherent scatter spectra that has been previously proposed is that they are due to enhanced plasma temperatures resulting in larger ion-acoustic speeds (Fejer et al., 1986). Though hypotheses for the cause of Type III and Type IV have been suggested by St.-Maurice and Chau (2016) with complementary measurements, further analysis is currently underway with ICEBEAR. ICEBEAR is able to measure all four different types of E-region coherent scatter, and in particular Huyghebaert et al. (2019) presented that they can occasionally all be observed in the same 5 s scan.

1.2. ICEBEAR

ICEBEAR is a recently deployed E-region coherent scatter radar that has been operated on a campaign basis (Huyghebaert et al., 2019). It makes coherent scatter measurements of the E-region ionosphere over a 600 × 600 km FOV and used a 10-antenna one-wavelength (1 $\lambda{\sim}6.06$ m for ICEBEAR) spaced linear receiving array from December 2017 to May 2018. The receiving array of the radar has since been reconfigured into a two dimensional (2D) pattern, though this publication focuses on the operations using only the initial linear array. The bistatic radar has a FOV located over northern Saskatchewan in Canada (centered on 58°N, 106°W), with the transmitter located at 50.893°N, 109.403°W, and the receiver located at 52.243°N, 106.450°W. The center frequency of ICEBEAR is 49.5 MHz. Received ionospheric scattered signals measured by the radar provide simultaneous details on the angle of arrival in azimuth, the signal-to-noise ratio (SNR), the Doppler shift, and the total signal propagation distance of the incoming signal through the utilization of a pseudo random noise (PRN) phase modulated code on the carrier signal. For a detailed description of the ICEBEAR system, see Huyghebaert et al. (2019).

In Huyghebaert et al. (2019), a preliminary angle of arrival determination was performed using only the shortest baseline cross-spectra from the receiving array to map the scatter. This analysis is expanded upon in this publication by including the cross-spectra data from longer baselines in the receiver antenna array to obtain a more accurate measurement of the location and size of the ionospheric scattering volume. The improved determination of the size and location of the scattering volume allow for a better understanding of the spatial extent of the plasma turbulence occurring in the E-region ionosphere.

1.3. Past Ionospheric Interferometry Studies

Previous researchers have investigated different methods to map ionospheric scatter in a radar field-of-view. A detailed description on the theory behind mapping ionospheric scatter using the cross-spectra between antennas can be found in Woodman (1997) and in Thompson et al. (2017). The ionospheric plasma perturbations measured by coherent scatter radars are considered to be a spread target where the scattering volume can exist over a large portion of the field-of-view. Signals from multiple directions can arrive simultaneously at the receiver, making the imaging of such a volume complicated but possible with a sufficient number of antennas. The number of antennas required to accurately represent the incoming signal will depend upon the complexity of the power distribution with respect to the elevation and azimuthal angle of arrival. The power distribution of the signal with respect to the angle of arrival is also known as the

brightness distribution. The reconstruction of the brightness distribution is accomplished by analyzing the coherence between signals arriving at different antennas at the receiver site. Some examples of determining the spatial extent of E-region plasma density perturbations through interferometry can be found in Hysell and Burcham (2000) and Meyer and Sahr (2004).

Chau and Woodman (2001) compared different methods of imaging ionospheric scatter using the Jicamarca Radio Observatory antenna array. Some of the methods included Fourier beamforming, Capon beamforming (Capon, 1969), Maximum Entropy (MaxEnt) beamforming (e.g., Hysell, 1996) and Gaussian blob imaging. From these methods, the Gaussian blob model appeared to provide the highest angular resolution for the high SNR data, though it required stringent prior assumptions on the data, such as the initial conditions for fitting and that the brightness distribution follows a Gaussian distribution (Chau & Woodman, 2001). Other studies investigating imaging techniques include one by Hysell and Chau (2006) in which data inversion methods were investigated for aperture synthesis radar imaging using the MaxEnt imaging method, and another one by Harding and Milla (2013) in which the relatively new technique of compressed sensing for ionospheric radar systems was investigated. Hysell et al. (2019) compared some of these different techniques, including Capon, MaxEnt, and orthogonal matching pursuit (compressed sensing), and determined that MaxEnt typically outperformed the other imaging methods investigated, though a Gaussian distribution fit similar to that done in Chau and Woodman (2001) was not included in the analysis.

1.4. The Present Study

After taking the previous studies into consideration, a Gaussian distribution fitting model, or Gaussian "blob" model, was selected. The reason for choosing this method but not Capon, MaxEnt, or compressed sensing, was to obtain values for the azimuthal angle of arrival and extent of the scattering volume based on the coherence values measured by the ICEBEAR receiver array in a single step. Deriving these values would require the estimation of the image first if other imaging methods are used. As well, as shown by Chau and Woodman (2001), fitting the data to pre-determined distributions can provide greater angular resolution than the other imaging techniques, so long as the initial conditions and assumptions are well defined and valid.

For the present study, a single Gaussian distribution was used to fit the cross-spectra coherence data for the scattering volume. Using a Gaussian image distribution to fit interferometric radio measurements is a common practice in radio astronomy (e.g., Thompson et al. (2017) and references therein) and can be applied to ionospheric scattering volumes as well, as shown by Chau and Woodman (2001). Using a single scattering volume when imaging can be accomplished as the ICEBEAR system is able to simultaneously measure range and Doppler velocity with relatively high resolution (~1.5 km range resolution, 10 Hz Doppler frequency resolution) and analyzes each measurement corresponding to the range-Doppler pair separately. More of the observation information available from the receiving array was used in this study compared to the previous one in Huyghebaert et al. (2019) by including all the cross-spectra measurements in the angle of arrival determination. Including this information increases the resolution and accuracy of the derived angle of arrival of the scatter, as well as providing details on the size, or extent, of the scattering volume in the azimuthal plane. A description of how the cross-spectra are used to obtain the spatial coherence and determine the location and size of the ionospheric scattering volume for ICEBEAR is provided below, including why these parameters are valuable for E-region research.

2. Modeling the Expected ICEBEAR Cross-Spectra Coherence Characteristics

To obtain an image from the cross-spectra measurements from ICEBEAR the Van Cittert–Zernike theory for interferometry is used (Thompson et al., 2017; Zernike, 1938). This theorem states that the coherence between antennas configured in two-dimensions in a planar array is related to the image brightness distribution in the sky through the equation:

$$V(u,v) = \int B(l,m)e^{-j2\pi(ul+vm)}dldm, \tag{1}$$

where $V(u, v)$ are the visibility, or coherence, values measured between two antennas, l is the direction cosine along the x-axis, m is the direction cosine along the y-axis, u is the spatial distance between antennas

in wavelengths along the *x*-axis, and *v* is the spatial distance in wavelengths between antennas in the *y*-direction. The incident signal is assumed to be in the far-field of the interferometer array arriving approximately perpendicular to the array orientation. The vertical components for both the image and baselines are neglected, with the antenna array considered to be a planar array with all antennas at the same height. For the 7° East of North pointing direction of the linear antenna array configuration used in this study, the linear antenna array was arranged only along the *x*-axis, resulting in the *y*-axis components of the equation being zero. The *y*-axis is therefore in the direction of the radar boresight. This results in the equation for the visibilities becoming:

$$V(u) = \int B(l)e^{-j2\pi ul}dl, \tag{2}$$

where only the azimuthal angle of arrival and extent are considered with respect to the *x*-axis. The brightness of the image can then be derived from the measured visibilities through the relation:

$$B(l) = \int V(u)e^{j2\pi ul}du. \tag{3}$$

A description of how the coherence values, $V(u)$, to be used in this equation are obtained from ICEBEAR measurements follows.

2.1. ICEBEAR Measurements of Spatial Coherence

The ICEBEAR cross-spectra are calculated from the received digitized complex voltage data in HDF5 format and stored in files also using the HDF5 format (The HDF Group, 1997-2020). The processing speed of the cross-spectra has been improved from previous operations described in Huyghebaert et al. (2019) by implementation of a graphics processing unit (GPU). The transition from a single i7 core to a modern GPU provided a reduction in processing time of ~48x. This provided the means to process the 45 unique cross-spectra in faster than real time for ICEBEAR. For this study only a single evening of data is presented during an active ionospheric period, although other days were processed and produced similar results. Processing the complex voltage data into the corresponding cross-spectra greatly reduces the data volume required to generate the visibility values and allows faster reprocessing times of the visibility values and corresponding imaging model fits. The cross-spectra of each antenna with itself were also determined and are referred to as the spectra. The processed spectra and cross-spectra for the day analyzed (March 10, 2018) in the HDF5 format can be found on Zenodo (Huyghebaert & Hussey, 2020).

Each of the receive paths from the antennas were phase matched in hardware to within 50° of each other, where the remaining phase offset was corrected in software. The phase differences could be from a multitude of possible sources, such as the pre-amplifiers, bandpass filters, external coaxial feedlines, internal coaxial connections and/or RF connectors. The receive path phase differences at 49.5 MHz were determined using a network analyzer, where the path measured was between the antenna and the Ettus Research X300 transceiver. For more information on the receive path and general setup of the ICEBEAR system, the reader is referred to Huyghebaert et al. (2019).

Spectra and cross-spectra values are obtained for every range-Doppler pair in a measurement period, which was set as 1 s for this study. ICEBEAR accomplishes the separation of the incoming signal into range-Doppler pairs with resolutions of ~1.5 km and 10 Hz through use of a continuous-wave (CW) coded signal and the associated processing of this signal. Details of this process are provided in Huyghebaert et al. (2019). The SNR for each range-Doppler pair were determined as an average from the spectra of the nine antennas used in the study. Only 9 of the 10 ICEBEAR receiver antennas were used as one antenna at the edge of the array was determined to have feedline issues. The SNR for each range-Doppler bin for each spectra was calculated with the equation:

$$SNR = \frac{P - N}{N} \tag{4}$$

where *P* is the total signal power for that range-Doppler pair and *N* is the noise, which was taken as the median of the full range-Doppler spectra for the averaged time period. As a result, the noise value calculated by this method will include some self-clutter bias during periods of high SNR due to the CW phase-modulated

signal utilized by the radar. The signal to self-clutter floor is ~27 dB for the ICEBEAR coded signal. Periods when there is self-clutter in the signal will raise the "noise" floor and can bias and/or mask the measurements of weaker signals, therefore one should be cognizant of the potential self-clutter bias during periods with large SNR values. An attempt at removing the self-clutter from the cross-spectra data is performed in this study and will be described later.

A 1.0 dB SNR threshold was set for calculating the ionospheric scatter azimuthal angle of arrival and spatial extent. This improves the imaging processing time, and neglects imaging values that are approaching the noise level. The process of fitting the azimuthal angle and extent was performed for each range-Doppler pair that exceeded this SNR threshold.

The visibilities for the linear antenna array, V, were calculated as the coherence between two antennas for a given range-Doppler pair for different antenna spacings. The coherence measurement for each range-Doppler pair is described by the equation:

$$V_{meas,corr}(f,r) = \frac{\langle v_1(f,r)v_2^*(f,r)\rangle - \langle v_{1,clutter}v_{2,clutter}^*\rangle}{(|\langle v_1(f,r)\rangle| - |\langle v_{1,clutter}\rangle|)(|\langle v_2(f,r)\rangle| - |\langle v_{2,clutter}\rangle|)}$$

(5)

where $v_1(f, r)$ is the complex measurement point of the spectrum at one antenna for a given frequency, f, and range, r, and $v_2(f, r)$ is the complex measurement point of the spectrum at another antenna for the same frequency and range. The asterisk, *, corresponds to the complex conjugate of the value. The effect of noise on the visibility measurements was considered in the calculation through the $v_{1,\text{clutter}}$ and $v_{2,\text{clutter}}$ terms. The noise contaminates the coherence values resulting in a typically lower coherence value than the signal alone would have due to the noise being decorrelated between antennas. $V(0)$ was set to 1.0, as the coherence of a signal with itself is 1.0. Possible reasons for the noise value to be coupled between antennas include sky noise and self-clutter of the coded CW signal. An attempt at removing these effects is performed using the v_{clutter} terms in Equation 5, where this term is calculated as the average of the first 100 range gates (150 km) of the processed spectra and cross-spectra. As the receiver and transmitter site are separated by ~240 km, the first 100 range gates should only consist of self-clutter and noise. By subtracting this value from the calculated visibility values, the portion of the self-clutter and sky noise that is coherent between antennas is removed. While simple, this method is computationally efficient and is a first order attempt at removing the effects of self-clutter and sky noise from the imaging results. The correction of the visibilities by Equation 5 will effectively narrow the azimuthal extent of the scatter and will reduce the chance of self-clutter and sky noise contaminating the results.

For each antenna pair, a visibility value is generated, which corresponds to the difference between the antenna positions. The relationship between the visibility values and the difference between the positions can be used to map the scatter. Here only a linear antenna array is used, so the positions of the antennas are along the x-axis with 1 λ spacing. The visibilities are henceforth listed as a function of the distance along the x-axis, or u, corresponding to a variable of $V(u)$. The dependence on range and Doppler frequency is left out for simplicity.

An example of measured visibility values for ICEBEAR is provided in Figure 1. This figure corresponds to a single range-Doppler measurement, where the range resolution is nominally 1.5 km and the Doppler frequency resolution is 10 Hz. If more than one antenna pair baseline corresponded to the same baseline length, also known as the spatial lag, an average of those coherence values was taken. For example, the one-wavelength baseline has eight samples which were averaged to obtain the value shown in Figure 1. The top panel in Figure 1 presents the magnitude of the coherence between two antennas while the bottom panel presents the phase of the coherence. This process was performed for all range-Doppler bins that exceed the SNR threshold for a given 1 s scan. The magnitude of the coherence can be related to the spatial extent of the scattering volume, while the phase can be related to the angle of arrival of the center of the volume.

For the analysis, the complex values of the visibility are used rather than the magnitude and the phase. This is to minimize the effect of phase wrapping on the derived angles of arrival and to produce a more accurate fit to the data. By using the component complex values both the magnitude and phase are considered simultaneously in the fitting process.
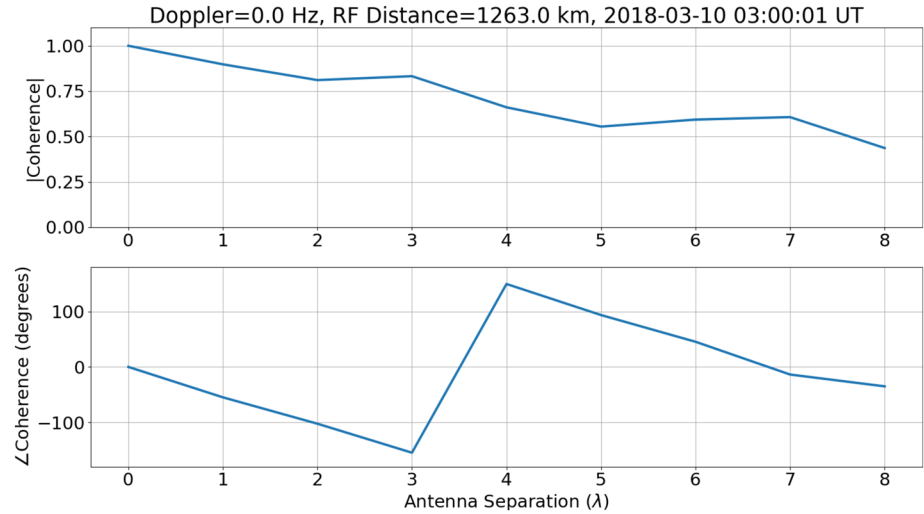
Figure 1. Spatial coherence measurements using ICEBEAR for a single range-Doppler pair. The top panel presents the magnitude of the coherence for the different baselines while the bottom panel presents the phase difference for the different baselines. ICEBEAR, Ionospheric Continuous-wave E-region Bistatic Experimental Auroral Radar.

2.2. The Gaussian Distribution Brightness Model

A Gaussian distribution model for the measured visibility values was implemented. As the signal is separated into range-Doppler bins of relatively high resolution, it is assumed that the measurements are originating from single scattering volumes for each range-Doppler bin. If there are multiple scattering volumes with the same Doppler shift at the same range the result will be a combination of the brightness distributions with the image characteristics weighted towards the volume with a stronger signal. For this experiment the ICEBEAR transmitter transmitted from two antennas creating a three lobe beampattern spanning across the receiver FOV. For plasma density irregularities spanning large extents in azimuth this will result in two distributions appearing in the image due to the transmitter beam nulls. As a single Gaussian model is utilized in the analysis, the azimuthal angle of arrival will point to a location between the two distributions and will have a large azimuthal extent. For active ionospheric periods with extended plasma density irregularity regions, this is something to be considered when interpreting the results.

The relation of the visibility distributions to the ionospheric scatter angle of arrival and the spatial extent of the scattering volume are derived below. These equations describe how a Gaussian distribution in the visibility space corresponds to the location and extent of the brightness of the image, where the relationship between brightness and visibility was provided in Section 2. One can model the visibility measurements as,

$$V(u) = e^{j\phi u}e^{-\phi_w u^2},\tag{6}$$

where ϕ corresponds to the phase of the signal and ϕ_w corresponds to the decay of the coherence based on the spatial lag. Recall that u is the spatial distance between antennas in wavelengths along the x-axis. The brightness of the image, $B(l)$, as a function of the direction cosine along the x-axis, l, is given by,

$$B(l) = \int e^{j\phi u}e^{-\phi_w u^2}e^{j2\pi ul}du.\tag{7}$$

By evaluating the integral, the image brightness distribution is given by the equation,

$$B(l) = \sqrt{\frac{\pi}{\phi_w}}e^{-(2\pi l+\phi)^2/4\phi_w}.\tag{8}$$

The image brightness maximizes when $l = -\phi/2\pi$ and decays away from this point. The full width half maximum (FWHM) value can be calculated by determining where the image intensity is half that of the peak. This can also be considered as the 3 dB point of the scattering volume. This 3 dB point is given by,

Table 1
Values Used for a Lookup Table for the Gaussian Visibility Model for Fitting to Equation 9, Where ϕ is the Value Corresponding to the Azimuthal Angle, ϕ_w is the Value Corresponding to the Azimuthal Extent, x in the Final Column Corresponds to the Azimuthal Angle "Bin," and y Corresponds to the Azimuthal Extent "Bin"

Fit parameter	Smallest value	Largest value	Bins	Equation
Φ	$-\pi$	$149\pi/150$	300	$\pi(x - 150)/150$
ϕ_w	0	$(1999\pi/3{,}600)^2$	2,000	$[\pi(y/3{,}600)]^2$

$$l = \sin\theta = \frac{-\phi \pm \sqrt{4\phi_w \ln(2)}}{2\pi}. \tag{9}$$

By solving for θ, the azimuthal angle and extent of the ionospheric scatter can be determined when assuming a Gaussian distribution. In this case θ corresponds to the boresight of the antenna array. This process then provides a means to analyze the spatial characteristics of the ionospheric coherent scatter measured by ICEBEAR and accurately map the measurements to the FOV.

3. Implementation of the Gaussian Model With ICEBEAR Measurements

Using the visibility analysis detailed in Section 2.2, a lookup table was generated for multiple ϕ and ϕ_w combinations. The values used for ϕ and ϕ_w are provided in Table 1. The values cover a span of only $-30°$ to $30°$ in azimuth (θ). This is due to the wavelength spacing of the ICEBEAR receiver antenna array. Beyond an azimuth of $\pm30°$ the data will alias to the opposite side of the field-of-view. The lookup table analysis method was chosen to provide sufficient processing speed while obtaining the azimuthal angle and extent values with a global minimum least squares fit value, though this method does result in the azimuthal angle and extent values being quantized.

To determine the most likely value for the azimuthal extent and angle of arrival, a weighted least squares fit method was used. The least squares fit is calculated for each azimuthal angle and extent pair in Table 1 and the minimum value is chosen as the corresponding image descriptor. This provides the global minimum and does not risk converging to a local minimum. The downside, as mentioned, is that the azimuthal angle and extent are quantized. The equation used to calculate the weighted least squares fit is,

$$LSF = \sum_{u=1}^{8} w(u) \mid V_{meas,corr}(u) - V_{fit}(u) \mid^2, \tag{10}$$

where $w(u)$ is a weighting factor based on the number of averaged samples that went into that spatial lag ($w(u) = 9 - u$), u is the spatial lag, or baseline length, normalized to wavelengths, $V_{meas,corr}(u)$ are the measured average complex coherence, or visibility, values for a given spatial lag with the noise correction applied from Equation 5, and $V_{fit}(u)$ are the modeled complex visibility values based on the azimuthal angle and extent. It is reiterated that a weighted least squares fit was calculated for each azimuthal angle and extent pair to create an array of least squares fit values. These weighted least squares fit values were scaled according to the number of samples for the associated averaged visibility for a spatial lag, but no values for the variance of the calculated visibilities were included. The indices of the minimum of the *LSF* array correspond to the values for ϕ and ϕ_w where a Gaussian distribution of the visibility values was used. A figure of the least squares fit values is provided in Figure 2. Here, the fitting method converged to a minimum value at $\phi = -0.922$ and $\phi_w = 0.0185$ corresponding to an azimuthal angle of $-8.434°$ and an azimuthal extent of $4.180°$. The azimuthal angle and extent are obtained from substituting ϕ and ϕ_w into Equation 9. The corresponding angle and ϕ are both negative due to the antennas being ordered from East to West and the azimuthal angle being determined as East of North. The azimuthal angle of arrival orientation was confirmed with all sky imagery on a different evening through a comparison between the location of the coherent scatter and the location of the auroral optical emissions. The auroral optical emissions and coherent scatter were not expected to be coincident, but instead to be in nearby regions, which was observed in the data. An example of a study with optical and radio measurements of the aurora can be found in Hysell et al. (2012).

The least squares fit values are used to determine the Gaussian distribution parameters that most accurately fit the ICEBEAR visibility data. The visibility data do not include the variance of the spectra and cross-spectra used to calculate them and therefore the least squares fit values are only a relative value used to determine the best fit of a Gaussian distribution to the data. In future studies an analysis will be performed to
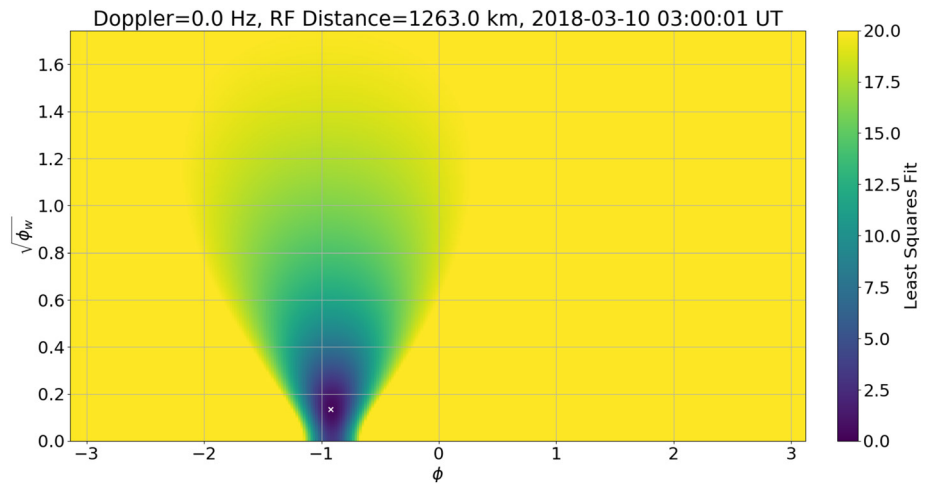
Figure 2. A plot of least squares fit values corresponding to ϕ and ϕ_w (Equation 9) for the coherence values shown in Figure 1. The minimum in the plot, represented by a white "x," corresponds to $\phi = -0.922$ and $\phi_w = 0.0185$. These values are used to determine the azimuthal angle of arrival and extent from Equation 9. The minimum value in the array corresponds to an azimuthal angle (θ) of $-8.434°$, an azimuthal extent of $4.180°$, and a least squares fit of 0.409.

include the variance details in the visibility calculations, which will contribute to providing physical meaning to the least squares fit values.

Once the values for the azimuthal angle and extent were determined the corresponding visibilities from Equation 6 were plotted with the measured data to compare the fit with the measured data. An example of this is shown in Figure 3. The figure shows that the method provides reasonable agreement between the fitted data and the real data.

There were many calculations for each range-Doppler bin above the SNR threshold as a least squares fit was calculated for every azimuthal angle and extent pair. Parallel processing was implemented to improve the speed of the calculations. Starting from the pre-processed cross-spectra and spectra data the azimuthal angles and extents were determined in a reasonable amount of time using the above technique, where processing time was dependent on the processing computer and the number of data points above the SNR threshold. In the case of March 10, 2018, with very active ionospheric activity over an extended portion of
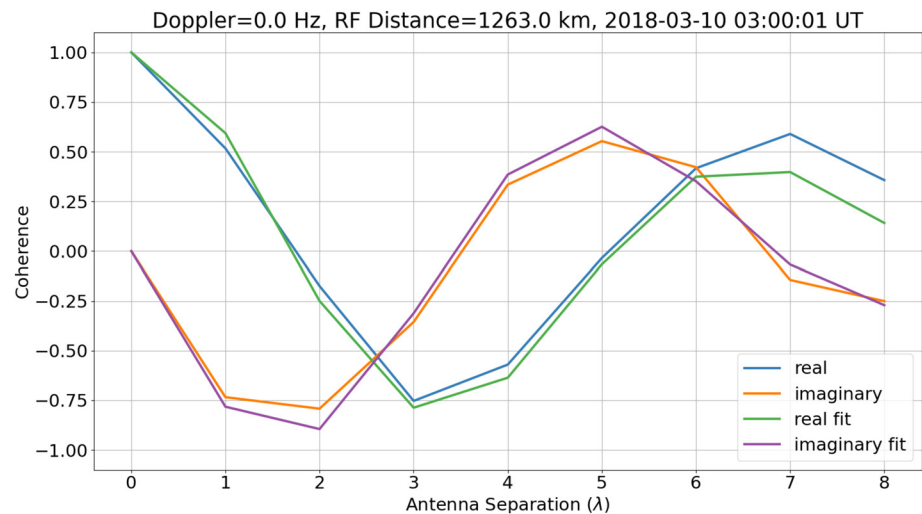

Figure 3. Figure 1 repeated with the Gaussian model fit included for the real and imaginary components of the cross-spectra coherence. The Gaussian model visibility values correspond to an azimuthal angle (θ) of $-8.434°$ and an azimuthal extent of $4.180°$.
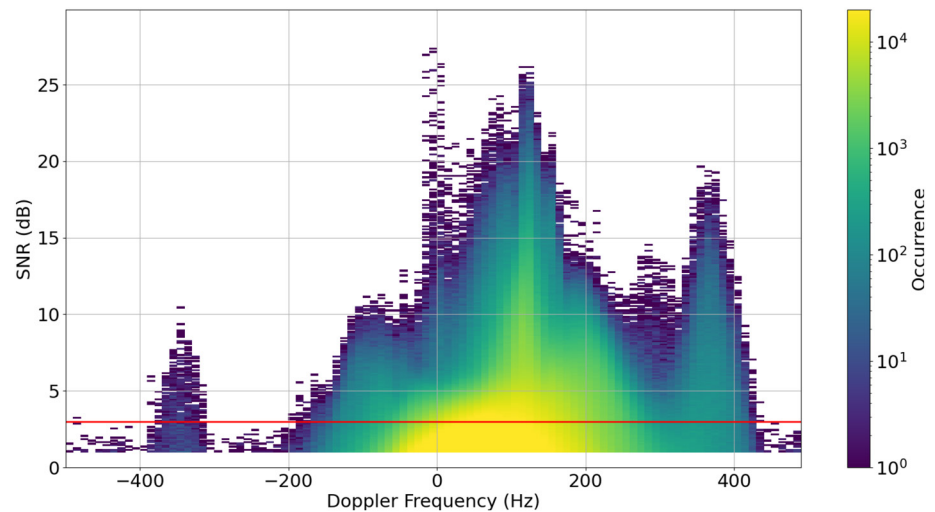
Figure 4. A histogram plot of the Doppler frequency and SNR of the ionospheric scatter. These quantities are not derived from the fitting routines described in this manuscript, but instead are determined from the averaged spectra of the antennas. To obtain the approximate Doppler velocity of the ionospheric scatter multiply the Doppler frequency by 3.03 m. The red line corresponds to a 3 dB threshold of the SNR, a commonly used value to eliminate weak signals. SNR, signal-to-noise ratio.

the evening (∼8 h), the image processing took ∼4 days. This was an extremely active period, and typically only a few days of this magnitude occur per month, with the majority of activity being constrained to a few hours in an evening. The processing of other less active days was considerably faster and was often faster than real time.

With the determination of the azimuthal angle and extent for ICEBEAR described, some important assumptions involved in the analysis are reiterated. These are that there is only a single region being scattered from in a given range-Doppler bin, that the visibility distribution follows a Gaussian distribution, and that the ionospheric scatter is relatively confined in elevation angle. The most suspect of these assumptions is that there is only a single scattering region.

When there is an occurrence of more than one scattering region the derived azimuthal extent of the scatter will be larger than any of the multiple individual regions and the derived azimuthal angle of arrival will be between the regions. Due to the coherent E-region scatter being separated into relatively high resolution range and Doppler bins with ICEBEAR, and each bin being individually fitted with a Gaussian distribution, it is expected that multiple scattering regions will occur infrequently. Even though infrequent, the scattering regions can consist of scatter with large spectral widths that overlap in Doppler frequency. Nulls in the transmitter beampattern can also create multiple scattering regions artificially, which must also be considered. As will be seen in the next section, there are occurrences of relatively large azimuthal extents that can be attributed to these factors.

4. Results From Azimuthal Angle and Extent Fitting

A single evening of data is presented, though other days were also processed and investigated. The other days investigated were less active, but displayed similar trends. The day that is presented was March 10, 2018, when the *Kp* index reached a value of 4 and ionospheric scatter was recorded throughout the evening (0–14 UT). The radar transmitted continuously throughout the time period. There are occurrences of dropped RF samples in the data, but these were infrequent (∼0.1%), grouped in time, did not affect the timing of the measurements, and were filtered out of the data before fitting.

To investigate the characteristics of the E-region coherent scatter occurring on March 10, 2018, the relationship between Doppler and SNR is plotted as a 2D histogram in Figure 4. The majority of the ionospheric E-region scatter has a positive Doppler shift and is therefore moving towards the radar. To obtain the
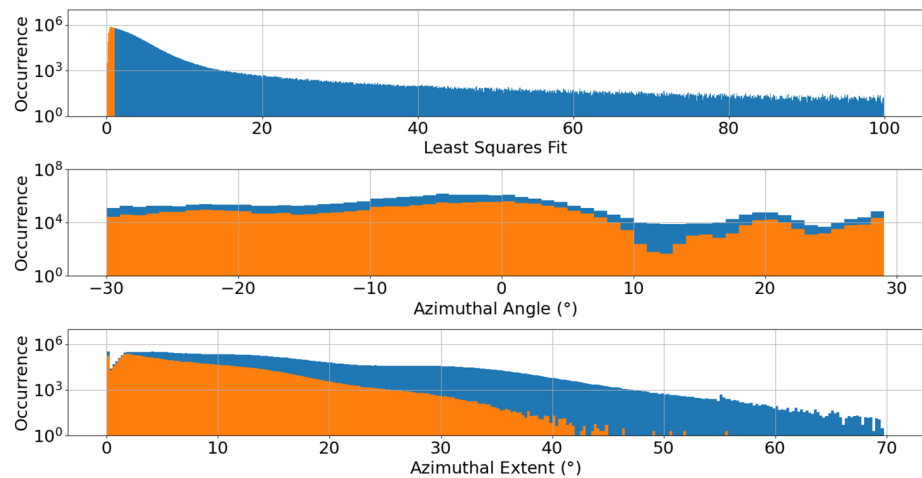
Figure 5. Histograms of the ICEBEAR coherence data fitted using a Gaussian distribution are presented from March 10, 2018. The orange histogram color represents an arbitrary least squares fit cutoff of 1.0, while the blue histogram color represents all the processed data. The top panel corresponds to the least squares fit of the data, the middle panel displays the azimuthal angle of arrival derived from the fitting routine, and the bottom panel displays the azimuthal extent of the scatter derived from the fitting routine. By only considering data with a relatively low least squares fit value, much of the large azimuthal extent data is removed. A potential explanation for the large azimuthal extent data corresponding to a poor fit is provided later in this section. ICEBEAR, Ionospheric Continuous-wave E-region Bistatic Experimental Auroral Radar.

Doppler velocity of the scatter one can multiply the Doppler frequency by ∼3.03 m, which corresponds to the half-wavelength of the operating center frequency of 49.5 MHz. This is an approximate Doppler velocity, as due to the bistatic nature of ICEBEAR the actual Doppler velocity will include a factor based on the angle of arrival and the bisector of the scattering geometry (e.g., Haldoupis & Schlegel, 1993). For scatter arriving from the westward portion of the FOV the value used to obtain the Doppler velocity would be ∼3.14 m. The bistatic nature of ICEBEAR has a relatively small effect on the Doppler velocity measured for the scattering geometries considered. The analysis presented in the current study to determine the angle of arrival of the scatter will contribute to providing refined Doppler velocity values for ICEBEAR in the future.

In Figure 4 it is evident that, while there are distributed peaks in the frequency/SNR space, much of the scatter transitions from one peak to the next with minimal to no gaps between the distributions. While labeling the different types of E-region coherent scatter has been done previously and makes for ease of description, the actual physical processes involved in generating the ionospheric plasma density irregularities may all be related to the Farley-Buneman plasma instability (e.g., St.-Maurice & Chau, 2016) with measurable transitions from one type to the next. The Type I E-region coherent scatter occurs at ∼±130 Hz, the Type II scatter occurs around 0 Hz Doppler shift, and the Type IV scatter occurs at ∼±300–400 Hz. Type III E-region coherent scatter is expected at ∼70 Hz, but does not show up as a distinct feature in Figure 4. This could be due to a low occurrence of Type III coherent scatter during this measurement period, with the occurrences unable to be isolated from the larger distributions without further analysis. The infrequent strong signals (>15 dB) at Doppler frequencies around 0 Hz are due to meteors. The red horizontal line in the plot corresponds to a 3 dB cutoff point for the data, which is a common SNR cutoff for usable data. The removal of this data would remove a large portion of usable data and is not performed in this study.

The azimuthal angle and extent data to be presented were derived from the same set of measurements that produced Figure 4. The Gaussian fitting method described in Section 3 was applied to the data to determine the azimuthal angle of arrival and extent of the E-region coherent scatter. From these data the spatial characteristics of the ionospheric scatter were investigated and are discussed below. There were 18,724,782 range-Doppler bins meeting the SNR threshold criteria of 1.0 dB after the removal of dropped samples.

Figure 5 contains the histogram distributions of the weighted least squares fit (top), the azimuthal angle (middle), and the azimuthal extent (bottom) for the Gaussian fitted visibility from March 10, 2018. The data with a least squares fit of less than 1.0 were also plotted in orange to show the results from filtering
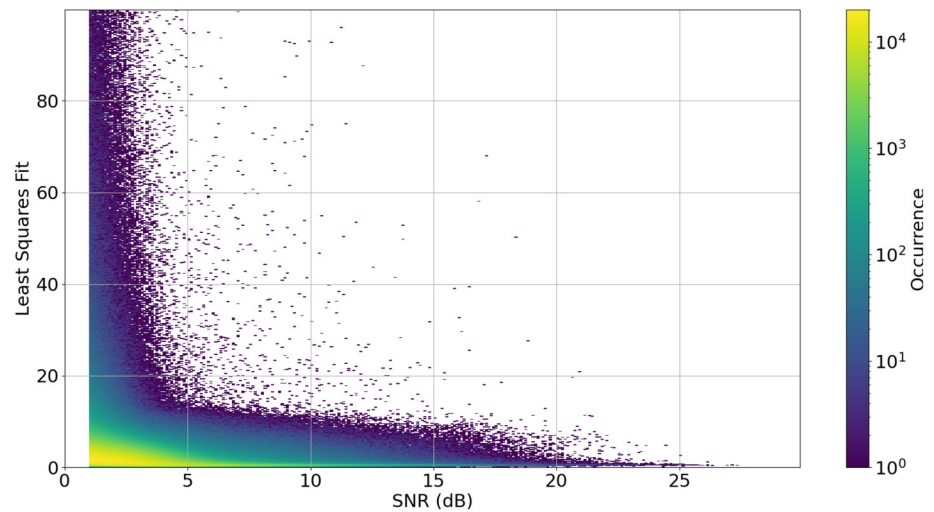
Figure 6. A two dimensional histogram plot of the least squares fit for the Gaussian distribution fitting method compared with the SNR of the incoming signal is presented. As expected, the least squares fit values decrease with increasing SNR, though do not reach 0. As this is a generalized model for the scatter, it is expected that it will not provide a perfect fit to the data. SNR, signal-to-noise ratio.

data with relatively good fits. Note that a logarithmic scale is used for the occurrence rate. The least squares fit occurrence of the full data set peaks between values of 0.4–0.5 and decreases with larger least squares fit values. The occurrence of larger least squares fit values do extend past the data shown, but continue to decrease with increasing least squares fit. As mentioned in Section 3, the least squares fit value used here only provides relative meaning in that it is only used to determine how closely the Gaussian distribution fit matches the measured data.

The amount of data points for a given azimuthal angle of arrival can vary due to a combination of the magnetic aspect conditions and the transmitter gain pattern, where two antennas separated by 3 wavelengths (~18 m) were transmitting the same signal. While ICEBEAR is capable of transmitting on 10 antennas at the transmitter site, due to the failure of an amplifier and the radio license restrictions only 2 antennas were transmitting for this experiment. The magnetic aspect conditions are ideal at a 100 km altitude slightly westward (negative azimuth) of the boresight of the array. This agrees with where the bulk of the ionospheric scatter measurements were located as presented in the middle azimuthal angle plot in Figure 5. The azimuthal extent does have a peak at 0° in the bottom panel of Figure 5, which corresponds to very small scattering volumes in the FOV. The resolution of the fitting technique could be increased for these narrow azimuthal extent values to obtain more accurate results at the expense of computation time. There is also an interesting increase in data at ~30° azimuthal extent that will be discussed further in this study.

The SNR was compared with the weighted least squares fit for the Gaussian visibility model to verify that the least squares fit values decrease with increasing SNR. As the SNR increases the model and data should more closely match, assuming the model is a valid representation of the data being fit. The results are presented as a 2D histogram in Figure 6. As expected, for increasing SNR the least squares fit values decreased. The least squares fit does not approach 0, but instead has some offset from 0 for large SNR. This could be due to the look-up table binning method implemented for the study resulting in an offset, due to the noise of the measurements not being fully accounted for, or due to a different model being required to produce a finely tuned fit to the real data, such as a multiple scattering volume model. As Gaussian distributions are commonly used in the literature (e.g., Chau & Woodman, 2001), this distribution was used in the determination of the azimuthal properties of the ionospheric scatter.

The distributions of azimuthal angle and extent were also investigated to determine if there was a relationship between the two quantities, providing potential evidence for a bias in the fitted distributions. Characteristics such as the type of E-region coherent scatter, the aspect conditions, and even the time of day can affect the azimuthal extent and where scatter is observed in the field-of-view. A 2D histogram of the
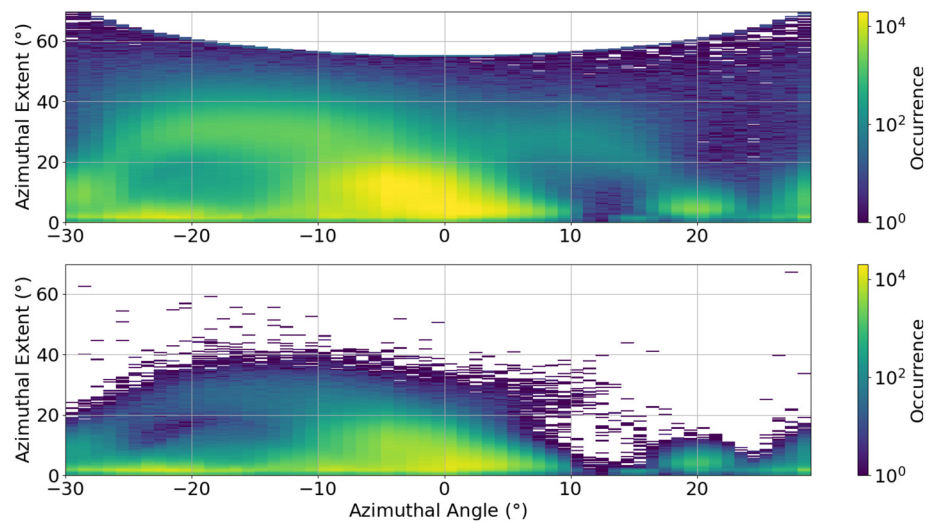
Figure 7. A two dimensional histogram of the azimuthal angle of the incoming signal compared with the azimuthal extent is presented. The top panel presents the whole data set for March 10, 2018, while the bottom panel uses an arbitrary least squares fit cutoff of 1.0. By incorporating this cut-off, the larger azimuthal extent values are diminished. See text for discussion.

azimuthal angle and extent is provided in Figure 7. The top panel presents the whole data set from March 10, 2018, while the bottom panel uses an arbitrary least squares fit cutoff of 1.0 for the fitted data on this day. The data were separated in this manner to demonstrate that many of the large azimuthal extents correspond to poor fits between the model and the data. The artifact that occurs for large azimuthal extents in the top panel where there is a crescent shaped lack of data is due to the binned values used for ϕ and ϕ_w. The range of values for ϕ_w could be extended, but this would cause an increase in processing time. From the bottom panel it can be observed that these very large azimuthal extents are due to poor fits to the model, so computation time was prioritized over the extension of the range of values for ϕ_w.

In both panels of Figure 7 a large distribution of scatter exists to the left of the boresight, which is expected due to the geomagnetic aspect conditions present in the field-of-view. The larger azimuthal extents could be due to the 3-lobe transmitter beampattern splitting the scattering region into two separate regions for extended plasma density irregularity regions due to the nulls in the beampattern. The large azimuthal extent distributions correspond to the increase in occurrence at 30° azimuthal extent mentioned earlier for Figure 5. In the future a broader beam with a more uniformly distributed power can be used for the ICEBEAR transmission signal, which will reduce the occurrence of the large azimuthal extent occurrences. The large azimuthal extents are reduced in occurrence when filtered by least squares fit values (bottom panel), providing credence to the hypothesis that the very large azimuthal extents are a result of the three lobe transmitter beampattern and that a multiple Gaussian blob fit is required to fit this data. The implementation of a multiple Gaussian fit would significantly reduce the resolution and/or increase the computation time of the fitting method. An investigation into accurate computationally efficient methods by which to implement a multiple Gaussian fit with recordable outputs is left for a future study. Filtering data based on the least squares fit values is a method by which to remove data that does not fit the single Gaussian distribution profile for the current implementation.

The fitting method described provides reasonable results, with the least squares fit values decreasing with increasing SNR and any possible discrepancies in the data able to be explained. The mapping of spread ionospheric targets for a bistatic system is a complex process and the analysis presented in this publication aims to produce a measure of the extent of the scattering volume for ICEBEAR that can be recorded with a manageable data storage requirement.
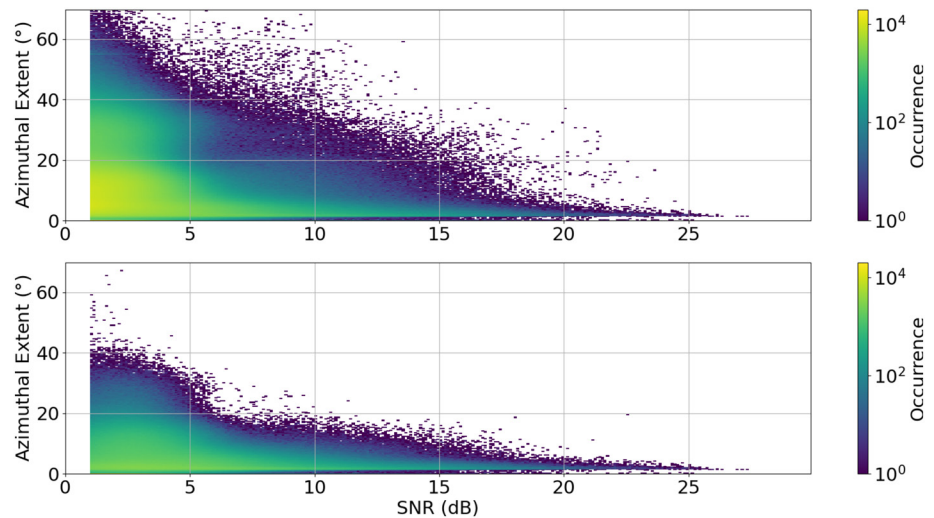
Figure 8. Histogram plots of the azimuthal extent of the ionospheric scatter derived from the Gaussian fit of the coherence values compared with the SNR. The top panel presents the whole data set from March 10, 2018, while the bottom panel uses an arbitrary least squares fit cutoff of 1.0. SNR, signal-to-noise ratio.

5. Discussion

Once the azimuthal angle of arrival and the azimuthal extent of scattering volumes were determined, the SNR and Doppler velocity of the incoming signal were compared to the azimuthal extent of the scattering volume. The data is shown in Figures 8 and 9. Similar to Figure 7, the top panels of both Figures 8 and 9 present the whole data set from March 10, 2018, while the bottom panels use an arbitrary least squares fit cutoff of 1.0. This was done to demonstrate the effects of removing poor fits of the Gaussian distribution model in the data.

In Figure 8 as the SNR of the signal increases, the range of values for the scattering area corresponding to the image FWHM point decreases. For signals with a large SNR the azimuthal extent of the ionospheric
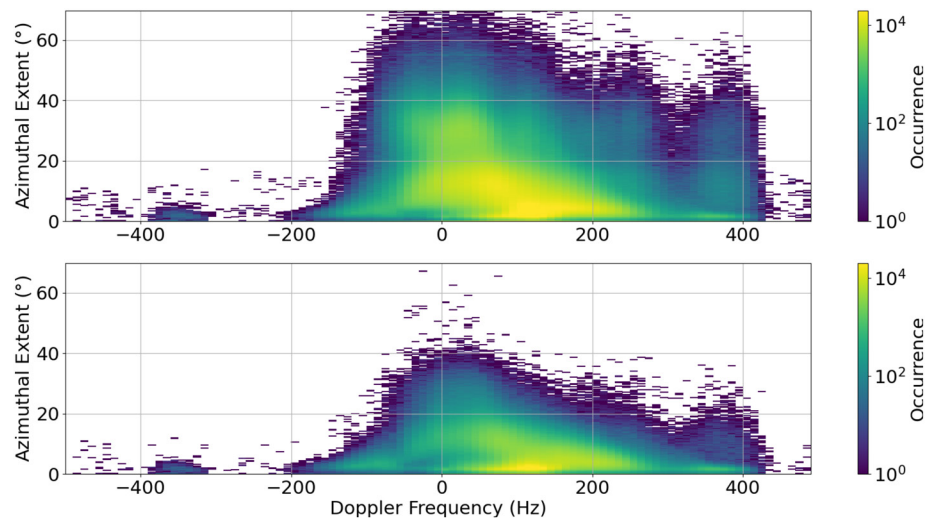

Figure 9. Histogram plots of the azimuthal extent of the ionospheric scatter derived from the Gaussian fit of the coherence values compared with the Doppler shift of the scatter. The top panel presents the whole data set from March 10, 2018, while the bottom panel uses an arbitrary least squares fit cutoff of 1.0. Due to the bistatic nature of ICEBEAR the Doppler frequency is used for the values along the x-axis, but to obtain an approximate Doppler velocity one can multiply the Doppler frequency by 3.03 m. ICEBEAR, Ionospheric Continuous-wave E-region Bistatic Experimental Auroral Radar.

scatter approaches a value in the range of 1.5°–1.75°. As also shown previously in Figure 7, this figure shows that the occurrence of large azimuthal extent data is diminished when filtering based on least squares fit values. The occurrence of high SNR, small azimuthal extent data is minimally affected by this filtering. The occurrence of the azimuthal extents of 30° is reduced by filtering based on least squares fit values, but does still exist, meaning that relatively large azimuthal extents can exist in the ICEBEAR data and are fit relatively well using a single Gaussian distribution.

In Figure 9, it is evident that ionospheric E-region scatter with a Doppler frequency of 0 Hz can have a large range of azimuthal extent values. The E-region coherent scatter with Doppler shifts of ∼0 Hz correspond to Type II E-region coherent scatter, though meteors are also included in this distribution. The meteors are expected to contribute to the small azimuthal extent distribution in the histogram, as ionospheric meteor trails are relatively localized (Ceplecha et al., 1998). The occurrences of Type II E-region coherent scatter with large azimuthal extents correspond to extended regions of plasma turbulence.

As the Doppler shift of the E-region coherent scatter increases, the occurrence of large azimuthal extent measurements decreases. From the lack of distinct boundaries between the different "Types" of E-region scatter, it is evident in the azimuthal extent data that characterization of the E-region coherent scatter into different types is a difficult endeavor, where the Type I distribution that is located at ∼130 Hz has no clear bounds in the data. The lack of bounds separating the types of scatter can be related to how the properties of the ionospheric E-region coherent scatter vary based on the flow angle of the ionospheric plasma with respect to the radar line of sight (e.g., Hysell et al., 2012). This previous study did not separate the scatter into types, but instead derived ionospheric parameters, such as the background electric field, based on the spectra of the E-region coherent scatter spectra measured.

In Figure 9, there are also distributions of the ionospheric scatter at Doppler frequencies of ∼±350 Hz that appear to be very localized, as well as cases of ionospheric scatter at Doppler frequencies of ∼350 Hz with relatively large azimuthal extents (5–20°). The large azimuthal extent and large velocity scatter distribution is interesting as it would imply that a very strong electric field is present in the E-region ionosphere over a large area at the time of this ionospheric scatter. This does not coincide with poor fits between the model and measured data, as the large azimuthal extents at a Doppler shift of 350 Hz still exist in the constrained least squares fit plot (bottom panel). This feature warrants further investigation in the future.

The implications of including the azimuthal extent when mapping scatter are presented in Figure 10, where 1 s of ICEBEAR data are presented. The top panel presents the ionospheric scatter mapped only using the azimuthal angle of arrival information, while the bottom panel presents the ionospheric scatter mapped using the half-power azimuthal extent that was derived for the ionospheric scattering volume. As may be expected, including the azimuthal extent of the scatter greatly increases the volume which the plasma density irregularities are considered to be located. The mapping of the azimuthal extent for this figure is performed by equally spacing 20 points for a given range-Doppler bin across the azimuthal extent centered on the azimuth angle of arrival. This method of mapping the data was utilized as means to demonstrate the importance of including the azimuthal extent when analyzing E-region coherent scatter, but does have the effect of having the final data plotted cover previously plotted data. Methods by which to improve the presentation of the large quantity of data are currently being investigated, but for the demonstration here this method proves sufficient. The preliminary result depicts a better representation of the size of the scattering volume than was previously performed in Huyghebaert et al. (2019) where only the azimuthal angle of arrival derived from single wavelength baselines to map the ionospheric scatter were used.

In Figure 10, the coherent scatter corresponds to three unique types: the green region of scatter closer to the radar is Type II; the blue region of scatter is Type I; and the very dark blue region of scatter is Type IV. The Type II scatter have a large azimuthal extent and are spread in the mapped data. The Type I scatter consist of both large and small azimuthal extents, while the Type IV scatter has a smaller azimuthal extent. It is interesting to note that the Type IV scatter appear to be much more secluded when refraining from plotting the azimuthal extent of the scatter compared to when the azimuthal extent is considered. That being said, even with the azimuthal extent included in the mapping of the data the Type IV scatter is localized in the FOV. It is evident that including the azimuthal extent is an important factor to consider to better represent how the different types of scatter fill the radar field-of-view.
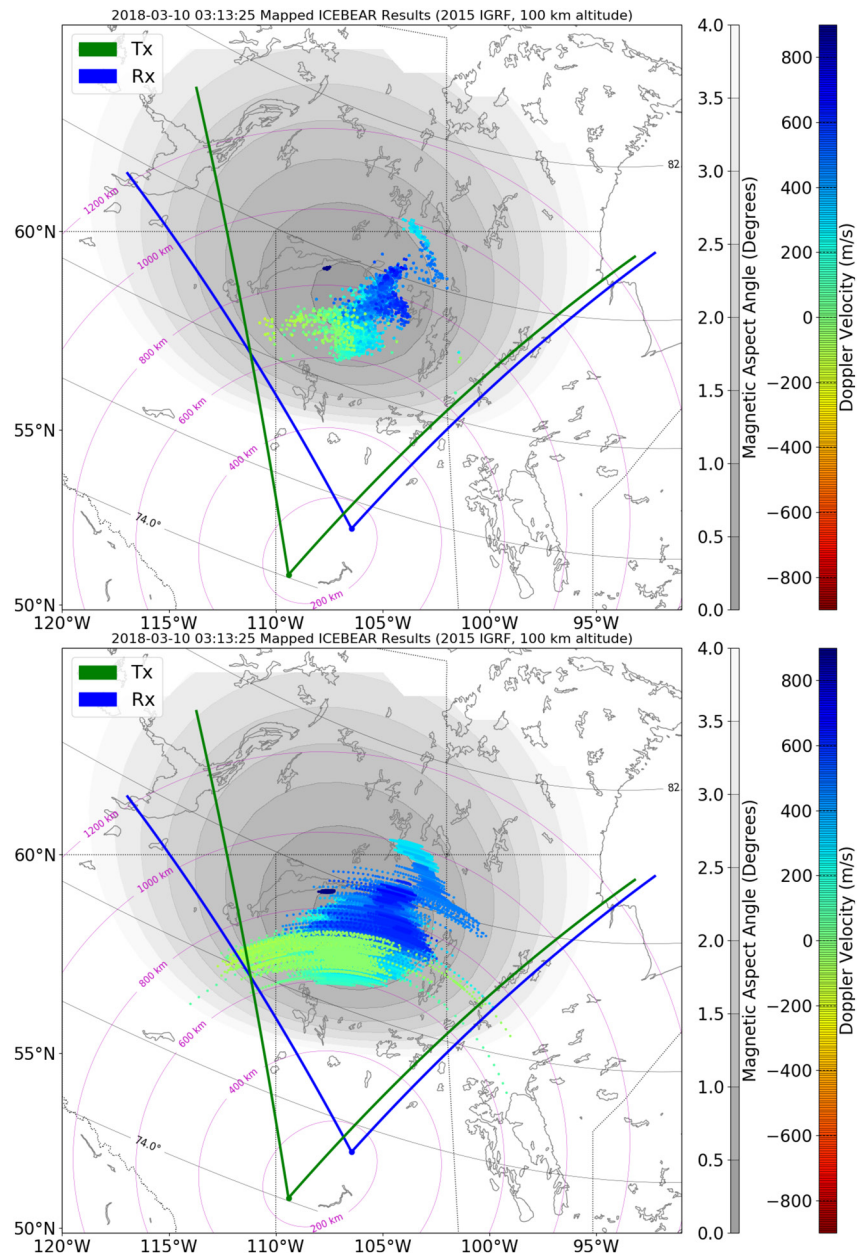
Figure 10. Example of mapping the scatter without (top panel) and with (bottom panel) the azimuthal extent included. The color of the scatter corresponds to the velocity, calculated as 3.03 m multiplied by the Doppler frequency. Type I, II, and IV ionospheric E-region scatter can be observed in the figure. It is clear that the azimuthal extent significantly increases the volume the ionospheric scatter is mapped to.

6. Summary/Conclusions

The image brightness distributions for ionospheric scatter from ICEBEAR have been determined by assuming a single scattering volume for the received signal for each range-Doppler bin for every 1 s ICEBEAR scan on March 10, 2018. The brightness distribution was modeled using a Gaussian distribution to describe the coherence of the measurements between antennas for a linear receiving array. From a least squares fit between the model and the ICEBEAR cross-spectra coherence data the azimuthal angle of arrival and the spatial extent of the ionospheric scatter were determined. The associated distribution of the SNR, Doppler frequency, azimuthal angle of arrival, azimuthal extent, and least squares fit were used to investigate potential biases in the data. It was found that large azimuthal extents commonly correspond to poor fits between

the single Gaussian distribution model and the ICEBEAR cross-spectra coherence data. This is able to be explained due to the ICEBEAR operating characteristics and the coherent scattering processes. For this experiment two antennas separated by 3 wavelengths were transmitting, producing a three lobe pattern with nulls in the FOV. These nulls potentially "split" some scattering volumes into two, effectively increasing the azimuthal extent of the scatter. The nulls approximately align with where there are large azimuthal extents. There was also the possibility of multiple scattering regions due to the ionospheric processes occurring. With proper error determination of the measurements these events can be more thoroughly characterized, though for the time being the least squares fit values can be used for filtering poor model representations of the data resulting in inaccurate angle of arrival information. As well, a general trend in the angle of arrival data was that the least squares fit decreases with increasing SNR, as is expected for an accurate model for fitting the data. In the future different transmission beampatterns can be used to reduce the effects of nulls with the imaging technique provided here. This can be accomplished by changing the distance between antennas, the number of transmitting antennas, and/or the phase and amplitude of the transmitted signal on each antenna.

It was shown that the azimuthal extent of the ionospheric E-region coherent scatter varies with respect to different Doppler frequencies and the SNR. The larger azimuthal extents correspond to lower SNR values, while large SNR scattering volumes are localized in the FOV. The azimuthal extent of the E-region ionospheric scatter at low Doppler frequencies has a large range of values, while at Doppler shifts greater than the ion acoustic speed the azimuthal extent is typically smaller. The histogram distribution presented in Figure 9 does not show significant separation between the different types of previously labeled E-region coherent scatter.

A comparison between the mapped data with and without the azimuthal extent makes it evident that the spatial extent of the ionospheric coherent scatter is an important parameter to consider when interpreting the data. The 1 s of ICEBEAR observations presented in Figure 10 displays the significance of the azimuthal extent, with Type I, Type II, and Type IV E-region coherent scatter presented. It is evident from the figure that by including the azimuthal extent details of the scattering volume while mapping the scatter the size of the region is significantly increased. Using the azimuthal angle and extent derived in the manner described allows ICEBEAR to accurately map the measured ionospheric coherent scatter in 2D space.

Future applications of this work include the implementation of accurate error bars for the angle of arrival with an inclusion of the variance in the ICEBEAR cross-spectra and spectra and a significant modification of the fitting routine, and the expansion of the current process to 2D spatial coherence space for the ICEBEAR reconfigured receiver array allowing the azimuthal and elevation extent of the ionospheric scatter to be determined. Science applications could include the determination of volumetric anomalous Joule heating correction factors due the Farley-Buneman instability from the spatial extent of the ionospheric coherent scatter and the determination of the direction and strength of fine scale electric fields in the E-region ionosphere using techniques such as those described in Hysell et al. (2012).

Data Availability Statement

The ICEBEAR spectra and cross-spectra data used in the analysis can be found on Zenodo (Huyghebaert & Hussey, 2020), where it is stored in HDF5 format.

References

Buneman, O. (1963). Excitation of field aligned sound waves by electron streams. *Physics Review Letters*, *10*, 285–287. https://doi.org/10.1103/PhysRevLett.10.285

Capon, J. (1969). High-resolution frequency-wavenumber spectrum analysis. *Proceedings of the IEEE*, *57*(8), 1408–1418. https://doi.org/10.1109/proc.1969.7278

Ceplecha, Z., Borovička, J., Elford, W. G., ReVelle, D. O., Hawkes, R. L., Porubčan, V., & Šimek, M. (1998). Meteor phenomena and bodies. *Space Science Reviews*, *84*, 327–471. https://doi.org/10.1023/A:1005069928850

Chau, J. L., & St-Maurice, J. (2016). Unusual 5 m E region field-aligned irregularities observed from northern Germany during the magnetic storm of 17 March 2015. *Journal of Geophysical Research: Space Physics*, *121*(10), 10316–10340. https://doi.org/10.1002/2016ja023104

Chau, J. L., & Woodman, R. F. (2001). Three-dimensional coherent radar imaging at Jicamarca: Comparison of different inversion techniques. *Journal of Atmospheric and Solar-Terrestrial Physics*, *63*(2), 253–261. https://doi.org/10.1016/s1364-6826(00)00142-5

Farley, D. T. (1963). Two-stream plasma instability as a source of irregularities in the ionosphere. *Physics Review Letters*, *10*, 279–282. https://doi.org/10.1103/PhysRevLett.10.279

Fejer, B. G., Providakes, J., Farley, D. T., & Swartz, W. E. (1986). Auroral E-region plasma waves and elevated electron temperatures. *Journal of Geophysical Research*, *91*(A12), 13583–13592. https://doi.org/10.1029/JA091iA12p13583

Haldoupis, C., & Schlegel, K. (1993). A 50-MHz radio Doppler experiment for midlatitude E-region coherent backscatter studies: System description and first results. *Radio Science*, *28*(6), 959–978. https://doi.org/10.1029/93rs01373

Haldoupis, C., Sofko, G., Hussey, G., & Mu, J. (1995). An overview of type-3 radar auroral research: Basic observational properties and new interpretation propositions. *Annales Geophysicae*, *13*(1), 10–24. https://doi.org/10.5194/angeo-13-10-1995

Hamza, A. M., & St-Maurice, J.-P. (1993). A self-consistent fully turbulent theory of auroral E-region irregularities. *Journal of Geophysical Research*, *98*(A7), 11601–11613. https://doi.org/10.1029/92ja02835

Harding, B. J., & Milla, M. (2013). Radar imaging with compressed sensing. *Radio Science*, *48*(5), 582–588. https://doi.org/10.1002/rds.20063

Hays, P. B., Jones, R. A., & Rees, M. H. (1973). Auroral heating and the composition of the neutral atmosphere. *Planetary and Space Science*, *21*(4), 559–573. https://doi.org/10.1016/0032-0633(73)90070-6

Huyghebaert, D., & Hussey, G. (2020). ICEBEAR spectra and cross-spectra data 2018-03-10. *Zenodo*. https://doi.org/10.5281/zenodo.3952548

Huyghebaert, D., Hussey, G., Vierinen, J., McWilliams, K., & St-Maurice, J. P. (2019). ICEBEAR: An all-digital bistatic coded continuous-wave radar for studies of the E-region of the ionosphere. *Radio Science*, *54*(4), 349–364. https://doi.org/10.1029/2018rs006747

Hysell, D. L. (1996). Radar imaging of equatorial F-region irregularities with maximum entropy interferometry. *Radio Science*, *31*(6), 1567–1578. https://doi.org/10.1029/96rs02334

Hysell, D. L. (2016). The radar aurora. Auroral dynamics and space weather. *Geophysical Monograph*, *215*, 193–209. https://doi.org/10.1002/9781118978719

Hysell, D. L., & Burcham, J. D. (2000). The 30-MHz radar interferometer studies of midlatitude E-region irregularities. *Journal of Geophysical Research*, *105*(A6), 12797–12812. https://doi.org/10.1029/1999ja000411

Hysell, D. L., & Chau, J. L. (2006). Optimal aperture synthesis radar imaging. *Radio Science*, *41*(2). https://doi.org/10.1029/2005rs003383

Hysell, D. L., Miceli, R., Munk, J., Hampton, D., Heinselman, C., Nicolls, M., et al. (2012). Comparing VHF coherent scatter from the radar aurora with incoherent scatter and all-sky auroral imagery. *Journal of Geophysical Research: Space Physics*, *117*(A10). https://doi.org/10.1029/2012ja018010

Hysell, D. L., Sharma, P., Urco, M., & Milla, M. A. (2019). Aperture-synthesis radar imaging with compressive sensing for ionospheric research. *Radio Science*, *54*(6), 503–516. https://doi.org/10.1029/2019rs006805

Kelley, M. C. (2009). *The Earth's ionosphere*. Academic Press. Retrieved from https://www.elsevier.com/books/the-earths-ionosphere/kelley/978-0-12-088425-4

Liu, J., Wang, W., Burns, A., Oppenheim, M., & Dimant, Y. (2018). Faster traveling atmosphere disturbances caused by polar ionosphere turbulence heating. *Journal of Geophysical Research: Space Physics*, *123*(3), 2181–2191. https://doi.org/10.1002/2017JA024746

Liu, J., Wang, W., Oppenheim, M., Dimant, Y., Wiltberger, M., & Merkin, S. (2016). Anomalous electron heating effects on the E region ionosphere in TIEGCM. *Geophysical Research Letters*, *43*(6), 2351–2358. https://doi.org/10.1002/2016gl068010

Lyon, R. F. (1997). Coherent radar imaging: Signal processing and statistical properties. *Radio Science*, *32*(6), 2373–2391. https://doi.org/10.1029/97rs02017

Makarevich, R. A. (2009). Coherent radar measurements of the doppler velocity in the auroral E region. *URSI Radio Science Bulletin*, *2009*(328), 33–46. https://doi.org/10.23919/URSIRSB.2009.7909539

Meyer, M. G., & Sahr, J. D. (2004). Passive coherent scatter radar interferometer implementation, observations, and analysis. *Radio Science*, *39*(3). https://doi.org/10.1029/2003rs002985

Moorcroft, D. R. (2002). Outstanding issues in the theory of radar aurora: Evidence from the frequency dependence of spectral characteristics. *Journal of Geophysical Research*, *107*(A10). https://doi.org/10.1029/2001ja009218

Rodger, A. S., Wells, G. D., Moffett, R. J., & Bailey, G. J. (2001). The variability of Joule heating, and its effects on the ionosphere and thermosphere. *Annals of Geophysics*, *19*(7), 773–781. https://doi.org/10.5194/angeo-19-773-2001

Sahr, J., & Farley, D. (1995). Three-wave coupling in the auroral E-region. *Annales Geophysicae*, *13*(01), 38–44. https://doi.org/10.5194/angeo-13-38-1995

Schlegel, K., & St-Maurice, J. P. (1981). Anomalous heating of the polar E-region by unstable plasma waves 1. Observations. *Journal of Geophysical Research*, *86*(A3), 1447–1452. https://doi.org/10.1029/ja086ia03p01447

St-Maurice, J.-P., & Chau, J. L. (2016). A theoretical framework for the changing spectral properties of meter-scale Farley-Buneman waves between 90 and 125 km altitudes. *Journal of Geophysical Research: Space Physics*, *121*(10), 10341–10366. https://doi.org/10.1002/2016ja023105

St-Maurice, J. P., Schlegel, K., & Banks, P. M. (1981). Anomalous heating of the polar E-region by unstable plasma waves 2. Theory. *Journal of Geophysical Research*, *86*(A3), 1453–1462. https://doi.org/10.1029/ja086ia03p01453

The HDF Group. (1997-2020). *Hierarchical data format*. http://www.hdfgroup.org/HDF5/

Thompson, A. R., Moran, J. M., & Swenson, G. W. (2017). *Van Cittert–Zernike theorem, spatial coherence, and scattering. In Interferometry and synthesis in radio astronomy*. Springer. Retrieved from https://doi.org/10.1007/978-3-319-44431-4_15

Wickwar, V. B., Lathuillere, C., Kofman, W., & Lejeune, G. (1981). Elevated electron temperatures in the auroral E-layer measured with the Chatanika Radar. *Journal of Geophysical Research*, *86*(A6), 4721–4730. https://doi.org/10.1029/ja086ia06p04721

Wiltberger, M., Merkin, V., Zhang, B., Toffoletto, F., Oppenheim, M., Wang, W., et al. (2017). Effects of electrojet turbulence on a magnetosphere-ionosphere simulation of a geomagnetic storm. *Journal of Geophysical Research: Space Physics*, *122*(5), 5008–5027. https://doi.org/10.1002/2016ja023700

Zernike, F. (1938). The concept of degree of coherence and its application to optical problems. *Physica*, *5*(8), 785–795. https://doi.org/10.1016/s0031-8914(38)80203-2